

An Agile Bicycle-like Robot for Complex Steel Structure Inspection

Son Thanh Nguyen¹, Hai Nguyen², Son Tien Bui³, Van Anh Ho³, Trung Dung Ngo⁴, Hung Manh La¹

Abstract—This paper presents a simple but compact design of a bicycle-like robot for inspecting complex-shaped ferromagnetic structures. The design concept for versatile locomotion relies on two independently steered magnetic wheels formed in a bicycle-like configuration, allowing the robot to possess multi-directional mobility. The key feature of a reciprocating mechanism enables the robot to change its shape when passing obstacles. A dynamic joint of the robot configuration makes it naturally adapt to uneven and complex surfaces of steel structures. We demonstrate the usability and practical deployment of the robot for steel thickness measurement using an ultrasonic sensor.

I. INTRODUCTION

Steel structures are indispensable parts of modern civilization. Typical structures, including bridges, wind turbines, electric towers, oil rigs, ships, and submarines, are made of steel. Frequent maintenance is required to warrant the safety and longevity of such structures [1]–[3]. Until today, these inspections are still manually conducted by professional human inspectors who visually inspect damages and detect faults on or inside these structures [4]–[6]. However, human-carried inspections are usually highly time-consuming, costly, and risky. For instance, it is highly dangerous for an inspector to climb up and hang on cables to inspect far-reached areas of bridges (Fig. 1a) or offshore oil rigs (Fig. 1b). Even the inspection of less complicated structures such as ship shells (Fig. 1c) and gas/oil tanks/piles (Fig. 1d) is also highly challenging due to its large scale.

Utilizing robots with sensing tools to automate inspection is an emerging solution [7]–[11]. Several innovative robot designs including conventional wheeled robots inspired designs [12]–[20] and tank-like tracks widening the contacting areas of the robots on steel surfaces [21]–[25] have been presented in recent years. Such designs can work well on structures with large surfaces, *e.g.*, ships or tanks but encounter difficulties on complex surfaces, *e.g.*, bridges and oil rigs. Inspired from the mobility capacity of climbing

This work is supported by the U.S. National Science Foundation (NSF) under grants NSF-CAREER: 1846513 and NSF-PFI-TT: 1919127, and the U.S. Department of Transportation, Office of the Assistant Secretary for Research and Technology (USDOT/OST-R) under Grant No. 69A3551747126 through INSPIRE University Transportation Center, and the Vingroup Joint Stock Company/ Vingroup Innovation Foundation (VINIF) under project code VINIF.2020.NCUD.DA094. The views, opinions, findings and conclusions reflected in this publication are solely those of the authors and do not represent the official policy or position of the NSF, the USDOT/OST-R, and the VINIF.

¹The authors are with the Advanced Robotics and Automation (ARA) Lab, Department of Computer Science and Engineering, University of Nevada, Reno, NV 89557, USA. ²Northeastern University, USA. ³Japan Advanced Institute of Science and Tech., Japan. ⁴University of Prince Edward Island, Canada. Corresponding author: Hung La, email: hla@unr.edu.

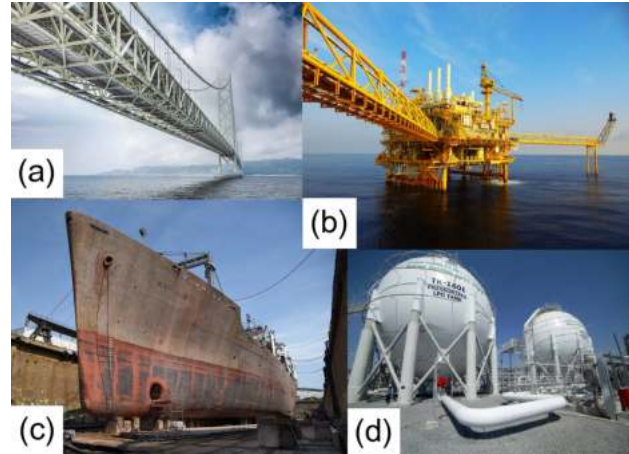


Fig. 1. Typical steel structures: a) Sea-crossing steel bridges. b) Offshore oil rigs. c) Ship shells. d) Oil tanks and pipelines. (Source: Google images)

animals, spider-like robot [26], legged robot [27], inchworm-like robot [28], and hybrid robot [29]–[31] were designed and examined. However, it is challenging to design a controller for the complexity of robot mechanics in real-world applications. Recent development of aerial robots provides an alternative inspection solution [32], [33]. Nonetheless, drones may be not feasible with installing touched sensors required for in-depth inspections of fatigue cracks or steel thickness of structures. Other non-standard moving mechanisms were proposed accordingly [34]–[36].

Nevertheless, priorly proposed bike-like robots do not have high directional flexibility, limiting mobility in narrow spaces. The rigid shapes of such robots restrict their maneuverability for passing extreme obstacles such as thin edges or acute corners. Except [37], these mechanic designs do not have a mechanism for touched sensors that are essential in structural inspection tasks, *e.g.*, measuring material thickness, paint quality, structural vibration.

This study focuses on optimizing the climbing capability and the multi-directional locomotion of a bike-like inspection robot, making it maneuver on complex ferromagnetic structures. Inspired from the work in [38], we developed a transforming mechanism enabling the robot to reconfigure to overcome concave and convex-edged obstacles such as L-, T-, and I-shaped beams or thorny corners. We also equipped the robot with a thickness sensor and a deploying mechanism. We demonstrated the robot’s working principles and functionalities through laboratory and field tests.

II. OVERALL SYSTEM DESIGN

The front view and the back view of the robot are depicted in Fig. 2a. We added a thickness transducer in the space

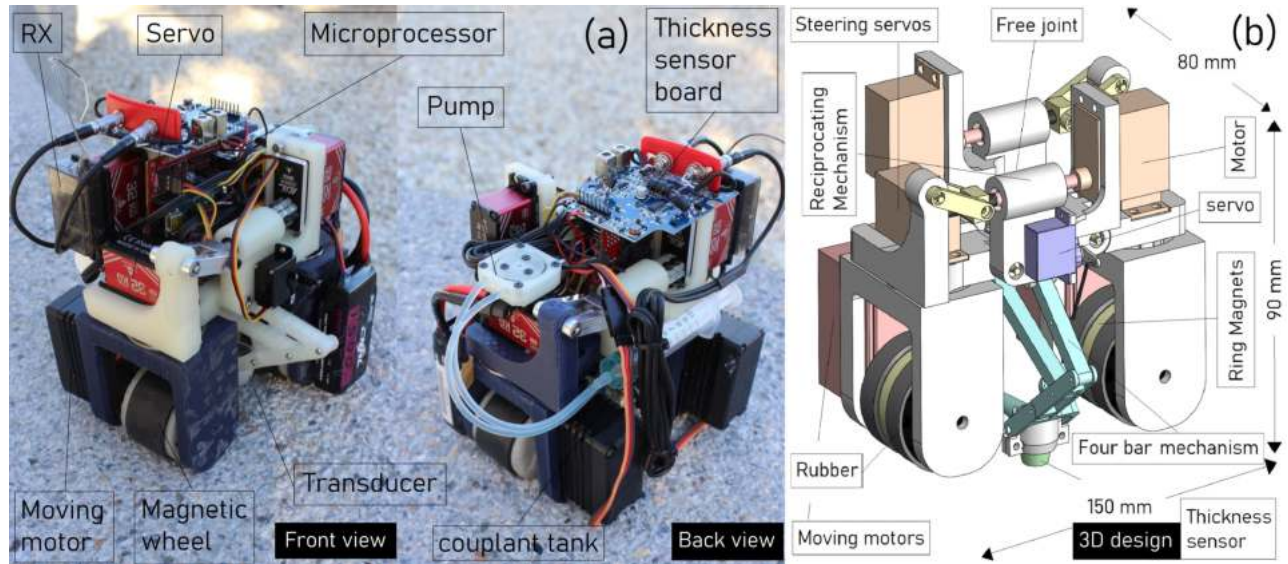


Fig. 2. (Left) The front and back view of the robot. (Right) The 3D design model of the robot.

between the two wheels. This location is ideal for protecting the sensor during the locomotion and allows good contact for measurements on both flat and curved surfaces. The robot's mass is 1.2kg , including the sensor. We used plastic to manufacture the lightweight robot chassis. When powered by a 700mAh LiPo battery, the robot can work for 30 minutes through remote control. Fig. 2b shows the overall mechanical design of the robot. The robot's dimension is $150 \times 80 \times 90\text{mm}^3$. We placed the ring magnets at the cores of the two rubber-covered wheels, driven by two high-torque gear DC motors ($100\text{kg}\cdot\text{cm}$ torque each). The steering actuators and transforming mechanisms are controlled by two servos ($32\text{kg}\cdot\text{cm}$ torque each). The front and the back of the frame are linked by a bearing acting as a dynamic joint.

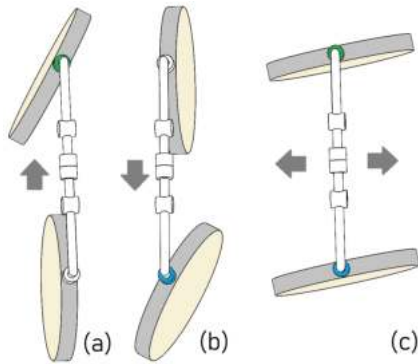


Fig. 3. The design concept shows the maneuverability of our robot with active joints for the front joint (green) and for the rear joint (blue). Two independent steering actuators allow the robot to enable bicycle-like moving modes (a) when only the front steering unit is activated and (b) when only the rear steering unit is activated to change the direction on narrow surfaces. When two steering units are activated simultaneously, (c) the robot can move sideways.

For high mobility, two revolute joints were installed, making two steering units (Fig. 3). These two units allow the robot to work on bicycle-like and multi-steering modes. The bicycle-like mode is utilized when the robot operates on

large surfaces with only one activated steering unit (Fig. 3a). On narrow surfaces, the robot can change the direction by activating the rear steering unit instead of the front one (Fig. 3b). In locations where sideways movements are required, the multi-directional mode is enabled. In this mode, two steering units are active simultaneously as in Fig. 3c. The maximum turning angle is kept at less than 90 degrees to maintain the robot's stabilization in this mode.

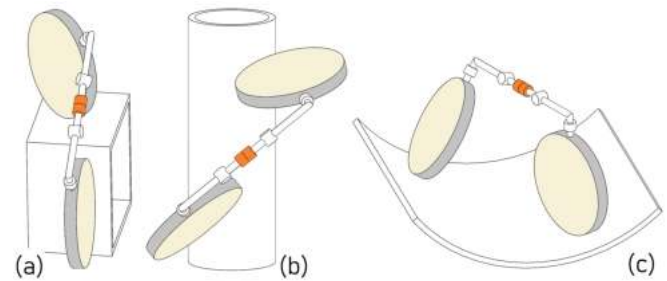


Fig. 4. The free joint (orange) in the middle of the robot's body helps its wheels better adhere to uneven surfaces, e.g., a) two flat curvatures, b) positive curvatures, c) negative curvatures.

In addition, a free joint (orange in Fig. 4) working as a dynamic connection between two halves of the robot's body allows the two wheels to stick to surfaces effectively, even uneven ones such as two flat curvatures (Fig. 4a), positive curvatures (Fig. 4b), or negative curvatures (Fig. 4c). Our design also enables the robot to pass thin edges and acute corners with two other revolute joints (shown in Fig. 5a-d). These two joints allow the distance between the two wheels to adapt to working surfaces (Fig. 5c-d).

III. MECHANICAL DESIGN AND ANALYSIS

This section provides a detailed mechanical analysis of our robot, including the analysis of the transformation, the maneuverability, and the sensor deployment mechanism.

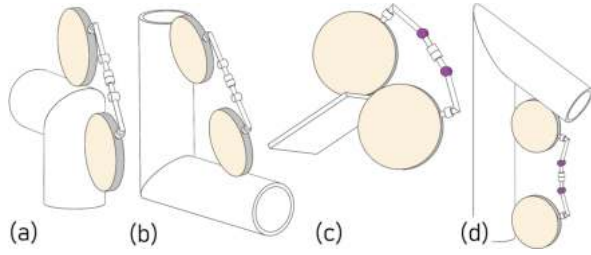


Fig. 5. Two revolute joints allow the two wheels' distance to be adjustable. In normal conditions *e.g.*, (a) and (b), the robot can pass corners without activating the two joints. When the two joints are activated (colored purple), the wheels' distance can be small to pass a thin edge (c) or big to pass an acute corner (d).

A. Robot Transformation Analysis

We used a reciprocating mechanism to adjust the distance between the two wheels. Due to the high load of attractive force when the two wheels are close, a feed screw is applied for the slider-crank part. The mechanism allows the robot to transform in three different shapes depending on particular situations, as shown in Fig. 6.

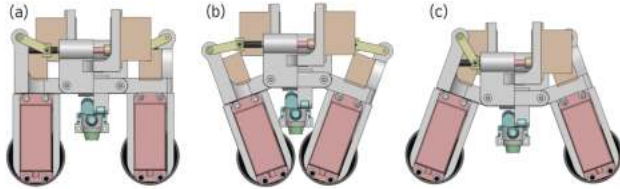


Fig. 6. The robot's shape when applying reciprocating mechanisms. a) in normal conditions, b) when passing thin edges, c) when passing acute internal corners.

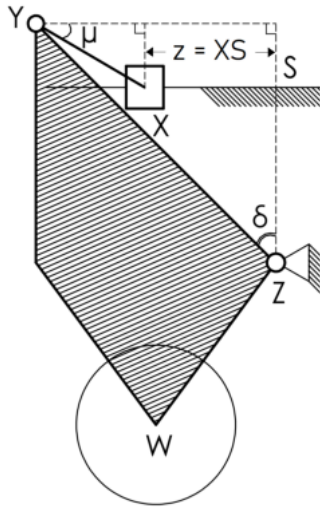


Fig. 7. The reciprocating mechanism's kinematic.

1) *Kinematic Analysis:* The kinematic is analyzed in Fig. 7, where W is the wheel center, reciprocating mechanism XYZ , and $z = XS$, we have:

$$XY \sin \mu = YZ \cos \delta - SZ, \quad (1)$$

$$XY \cos \mu = YZ \sin \delta - z. \quad (2)$$

Square then sum both sides of (1) and (2), we have:

$$XY^2(\sin^2 \mu + \cos^2 \mu) = (YZ \cos \delta - SZ)^2 + (YZ \sin \delta - z)^2. \quad (3)$$

Simplifying (3), we have:

$$SZ \cos \delta + z \sin \delta = \frac{z^2 + YZ^2 + SZ^2 - XY^2}{2XY}, \quad (4)$$

resulting in function $\delta = f(z)$, which is used to control the reciprocating mechanism of the robot.

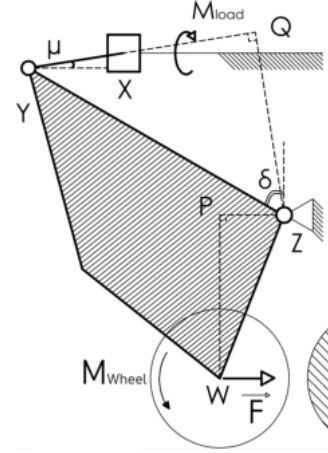


Fig. 8. Force analysis of the reciprocating mechanism.

2) *Force Analysis:* The robot's shape transformation is the combination of controlling δ (Fig. 8) and moving wheels simultaneously. The load (the magnetic force between the two wheels) is shared between the two wheels and the reciprocating mechanism. In Fig. 8, where F is the attractive force between the two wheels, M_{load} is torque that feeds screw bears, and i is the feed screw's transmission ratio, we have:

$$M_{load} = F \frac{PW}{QZ \cos \mu} i - M_{wheel}. \quad (5)$$

B. Robot Maneuverability Analysis

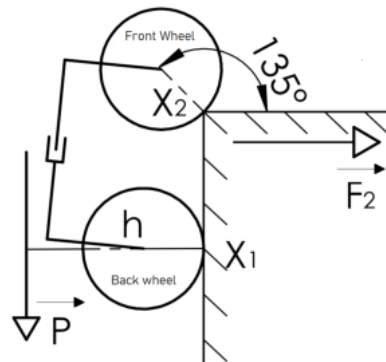


Fig. 9. A situation where the adhesive force is minimal, resulting in a high chance of falling over. In this case, the adhesive force of the front wheel is significantly reduced when the robot hits an edge.

1) *Adhesive Force:* To analyze the adhesive force required for the robot to climb on the steel structure under normal working conditions, we performed the analysis on an extreme situation where the adhesive force between the magnetic

wheels and the contacting structures is minimal, *e.g.*, Fig. 9. Here, X_1 and X_2 are two contact points of the back wheel and front wheel, respectively, P is the robot's weight, and h is the distance from the center of mass of the robot to X_1 . If F_2 is an adhesive force of the front wheel at X_2 , then F_2 is at its minimum when the front wheel hits the corner. To keep the robot safe, the following condition needs to be satisfied:

$$F_2 \cdot X_1 X_2 > Ph \rightarrow F_2 > \frac{Ph}{X_1 X_2}. \quad (6)$$

According to ISO 3691 [39] for safe weight lifting, a safety factor of 5 was selected. Therefore, the real adhesive force F_2 needs to be *at least five times greater than the result from the above theoretical calculation in (6)*.

2) *Extreme Locomotive Situations*: This analysis calculates the necessary motor torque when the robot stands the highest load. The highest load occurs when the robot passes an internal corner between two perpendicular surfaces (Fig. 10), the front wheel bears an additional force $F_{2,2}$, which is the adhesive force of the front wheel on the surface 2. Similarly, $F_{2,1}$ is the adhesive forces of the front wheel on the surface 1. F_{f2} is the friction of the front wheel on the surface 2, r is the wheel's radius, k is the static friction coefficient (between rubber and steel in our design). The minimum force of the front wheel that allows the robot to be able to overcome the corner must satisfy:

$$\frac{M_{\text{moving}}}{r} > F_{2,1} + F_{f2} + \frac{P}{2}. \quad (7)$$

Therefore, the moving motor torque needs to satisfy:

$$M_{\text{moving}} > r(F_{2,1} + kF_{2,2} + \frac{P}{2}). \quad (8)$$

According to IEC 60034 [40], the actual torque selected to be *at least double that of theoretical calculation in (8)*.

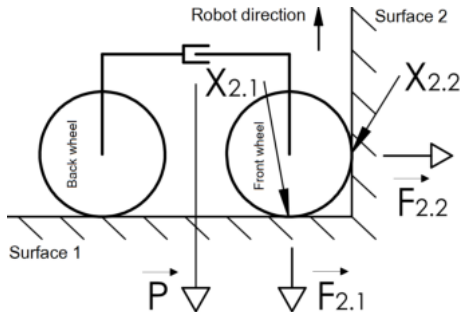


Fig. 10. When the robot passes an internal corner between two perpendicular surfaces, the robot's load increases significantly.

3) *Steering*: We also analytically investigated the load torque on the revolute joints. There are two mutually affected forces, named static friction and the attractive force at the two magnetic wheels, as illustrated in Fig. 11. Let F_{12} be the adhesive force of wheel 1 affecting wheel 2, and let F_f be the friction at X_2 , the measured load-force at point L (Fig. 11a) has to satisfy the following condition:

$$F_{12} + F_f < \frac{M_{\text{steering}}}{r}. \quad (9)$$

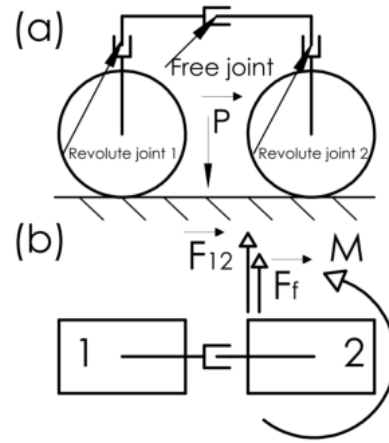


Fig. 11. An experiment is conducted to investigate the load on a steering servo motor. A dynamo-meter is mounted on one wheel's edge (point L) to measure the load. The distance from L to the rotating point X_2 is r (the wheel's radius). a) Side view. b) Top view.

Thus, the steering servo torque needs to satisfy:

$$M_{\text{steering}} > r(F_{12} + k(F_2 + P)). \quad (10)$$

Based on IEC 60034 [40], the actual servo's torque is chosen to be *at least two-fold compared to that of theoretical calculation in (10)*.

C. Sensor Deployment Mechanism Analysis

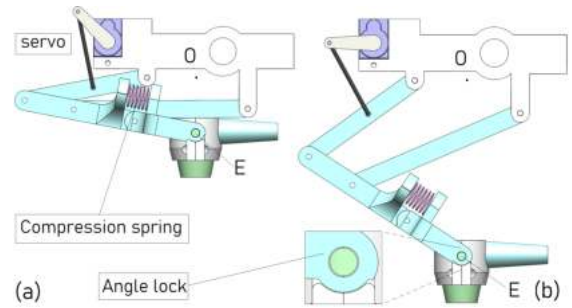


Fig. 12. The four-bar mechanism. A compression spring acts as a soft contact with the surface. An angle lock is added to create a free movement of the probe when approaching uneven surfaces.

A four-bar mechanism was designed for generating vertical movements of the transducer, as shown in Fig. 12. A compression spring was added together with an angle lock to avoid the overload of servo motors and enhance contact between the transducer and the inspection surfaces.

We analyzed the mechanism using a simplified model shown in Fig. 13, indicating that the target four-bar linkage ACDB can be considered as a special mix of the ACE and BDE reciprocating mechanisms with the same virtual slider E.

1) *ACE Analysis*: In Fig. 13, we have:

$$CE \cos \varphi = x - AC \cos \alpha, \quad (11)$$

$$CE \sin \varphi = AO + AC \sin \alpha. \quad (12)$$

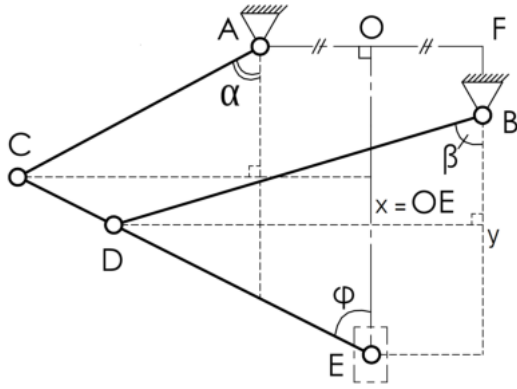


Fig. 13. The four-bar mechanism's kinematic.

Applying the similar approach as in (1) and (2) for (11) and (12), we have:

$$x \cos \alpha - AO \sin \alpha = \frac{x^2 + AO^2 + AC^2 - CE^2}{2AC}. \quad (13)$$

We see that (13) presents a function $\alpha = f(x)$.

2) *BDE Analysis*: In Fig. 13, we have:

$$BD \cos \beta = x - BF - DE \cos \varphi, \quad (14)$$

$$BD \sin \beta = OF + DE \sin \varphi, \quad (15)$$

$$\rightarrow y \cos \varphi - AO \sin \varphi = \frac{y^2 + AO^2 + DE^2 - BD^2}{2DE}, \quad (16)$$

where $y = x - BF$. Similarly, (16) presents a function $\beta = f(y)$.

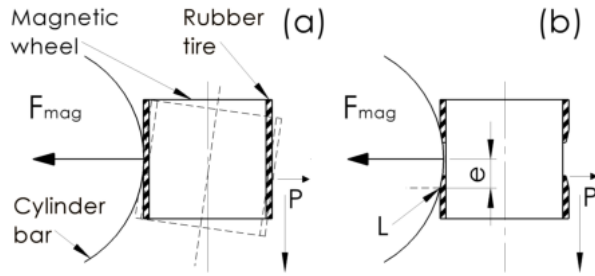


Fig. 14. The design of rubber tires. a) One strip tire, b) Two separated strips tire.

D. Wheel Tire and Couplant Pumping

1) *Wheel Tire Design*: The design requires a particular pattern to warranty the robot's stability in extreme situations, particularly when the robot's body is horizontal as it travels along a cylinder bar. Fig. 14 depicts a cross-section in this situation. With one strip of tire for the entire wheel, the robot's body is inclined because of gravity, causing drifting when the robot turns as illustrated in Fig. 14a. Two separated rubber strips were applied to improve the approaching area between the tire and curved surfaces to fix the drifting issue. As shown in Fig. 14b, using two strips, the turning point L is created, and the moment $F_{mag}e$ is generated to stabilize the robot's body.

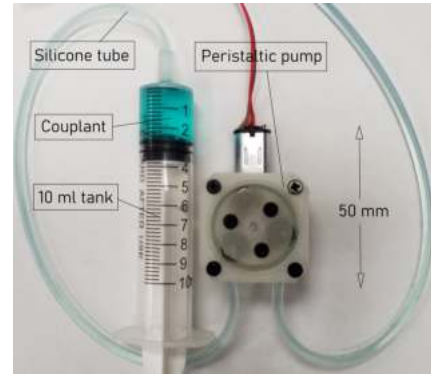


Fig. 15. High viscosity couplant is stored in a syringe tank. A mini peristaltic pump with a silicone tube is utilized to release the couplant.

2) *Couplant Pumping*: Since we used an ultrasonic sensor for thickness measurement, couplant is necessary to fill the air gap between the transducer and the test specimen. The couplant with high viscosity was utilized to stick well on surfaces, even in upside down or vertical positions. We have chosen the peristaltic pump type for high viscosity gel. We also chose the syringe mechanism for gel storage because it can work on any robot poses. The pump is described in Fig. 15.

IV. EXPERIMENTAL EVALUATION

We conducted experiments to evaluate the magnetic force created by the wheels and the climbing ability and failure avoidance. Based on condition (6) and ISO 3691 standard [39], the force measured by a force meter satisfied the tests of extreme situation as described in Fig. 5a, 9, and 14 with the smallest diameter of cylindrical bars being 100mm. In the worst-case scenario where there existed only one contacting point between the wheel and a surface, the adhesive force was 15N. The motors' power and the transforming mechanism's function were also validated in additional experiments, and conditions (5) and (8) were satisfied. The robot's mass $m = 1.2kg$, so the total weight of the robot is approximately $P = mg = 12N$ when we assume that the gravitational acceleration $g = 10m/s^2$.

TABLE I

SPECIFICATIONS OF OUR TESTING CONDITIONS.

| Structural parameters | Dimension (mm) |
|----------------------------------|----------------|
| Thinnest steel surface | 2 |
| Smallest steel cylinder diameter | 100 |
| Thickest coated paint | 3 |
| Highest nut or bolt area | 4 |

Both the indoor and field experiments were conducted on different steel structures and bridges and a few typical climbing examples are shown in Fig. 16, 17, and 19. The steel structures have different thicknesses of paint coating, and some of these surfaces are rusty, dirty, or still in minor-rusty conditions. Table I presents the specifications of our testing conditions. Details about laboratory tests' performances using an indoor structure and field tests on an outdoor steel bridge are highlighted below.

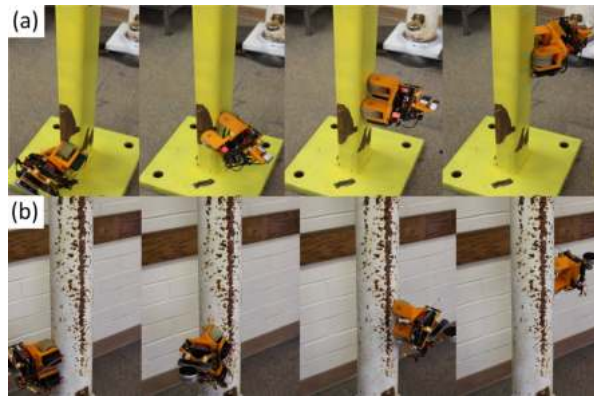


Fig. 16. Indoor locomotion tests on rectangular and cylindrical bars. Due to the flexible body and two wheels arrangement, the robot can fully contact and traverse every location of testing structures.

A. Laboratory Tests

We built an indoor structure comprising common parts of general steel structures (cylinder, L-, I-, U-shaped beams) with structural transition joints to validate the robot's locomotion functionalities. Our robot traversed smoothly to all locations in the testing structure. Fig. 16a-b show different steps when the robot was moving on a rectangular tube and a cylindrical shape, respectively.

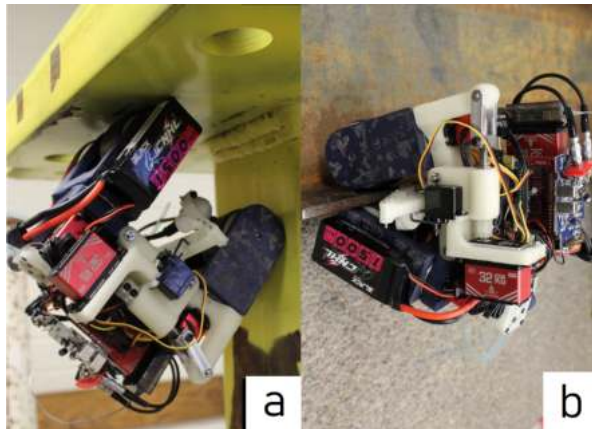


Fig. 17. The robot is passing convex and concave surfaces: a) turn of 90 degrees on internal corners. b) transforms the wheels to pass a thin edge on a U-shaped beam.

Fig. 17a shows the robot turned a 90-degree on an internal corner. When facing a thin edge, the robot changed its configuration by adjusting the distance between its wheels (Fig. 17b). Fig. 18 demonstrates a test of thickness measurement. The transducer with a nozzle on one end was first controlled to contact the target surface, then couplant was applied to the surface through the pump. The steel thickness was reported 27.5mm.

B. Field Tests

We deployed the robot together with the sensor on a cylindrical type bridge as shown in Fig. 19. The bridge's structure includes cylindrical surfaces of 30cm and 22cm diameters. The robot performed the thickness measurements

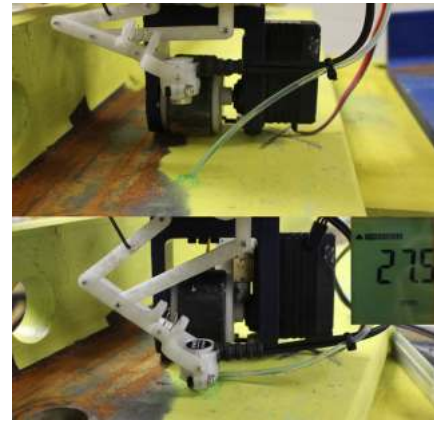


Fig. 18. A demonstration of measuring the thickness of a steel surface. The transducer is well contacted to the surface thanks to the compression spring and angle lock. The final result is averaged over three times.

in some rusty areas to check severe corrosion conditions. However, our sensor deployment mechanism could not reach the internal angles of some rusted spots due to the vertical height limit of the four-bar mechanism.



Fig. 19. The robot operates on a cylindrical steel bridge to perform thickness measurements and checking for corrosion.

V. CONCLUSIONS AND FUTURE WORK

In this paper, we have presented a design of a bicycle-like robot for inspecting steel structures. The robot can agilely climb different structures to perform a structural inspection. The design was validated on a laboratory testing structure and a cylindrical steel outdoor bridge. Experiments showed that the robot can adhere firmly to steel structures of various difficult levels. In this study, we provided a rigorous analysis of the kinematics and forces that set the theoretical foundation guaranteeing the operational capability of the robot in challenging applications.

In the future, the robot can be further equipped with non-destructive testing (NDT) sensing modules for more in-depth inspections of paint thickness, fatigue cracks, or structural vibration. Another interesting future direction is about adding advanced sensors and cameras for autonomous localization, navigation, and inspection (*e.g.*, using computer vision techniques) to fully automate the inspection task.

REFERENCES

- [1] S. Gibb, H. M. La, T. Le, L. Nguyen, R. Schmid, and H. Pham, "Nondestructive evaluation sensor fusion with autonomous robotic system for civil infrastructure inspection," *Journal of Field Robotics*, vol. 0, no. 0, 2018. [Online]. Available: <https://onlinelibrary.wiley.com/doi/abs/10.1002/rob.21791>
- [2] H. M. La, N. Gucunski, K. Dana, and S.-H. Kee, "Development of an autonomous bridge deck inspection robotic system," *Journal of Field Robotics*, vol. 34, no. 8, pp. 1489–1504, 2017. [Online]. Available: <https://onlinelibrary.wiley.com/doi/abs/10.1002/rob.21725>
- [3] S. Gibb, T. Le, H. M. La, R. Schmid, and T. Berendsen, "A multi-functional inspection robot for civil infrastructure evaluation and maintenance," in *2017 IEEE/RSJ International Conference on Intelligent Robots and Systems (IROS)*, 2017, pp. 2672–2677.
- [4] H. Ahmed, H. M. La, and N. Gucunski, "Review of non-destructive civil infrastructure evaluation for bridges: State-of-the-art robotic platforms, sensors and algorithms," *Sensors*, vol. 20, no. 14, 2020. [Online]. Available: <https://www.mdpi.com/1424-8220/20/14/3954>
- [5] H. Ahmed, H. M. La, and K. Tran, "Rebar detection and localization for bridge deck inspection and evaluation using deep residual networks," *Automation in Construction*, vol. 120, p. 103393, 2020. [Online]. Available: <https://www.sciencedirect.com/science/article/pii/S0926580520309730>
- [6] U. H. Billah, H. M. La, and A. Tavakkoli, "Deep learning-based feature silencing for accurate concrete crack detection," *Sensors*, vol. 20, no. 16, 2020. [Online]. Available: <https://www.mdpi.com/1424-8220/20/16/4403>
- [7] T. Le, S. Gibb, N. Pham, H. M. La, L. Falk, and T. Berendsen, "Autonomous robotic system using non-destructive evaluation methods for bridge deck inspection," in *2017 IEEE International Conference on Robotics and Automation (ICRA)*, 2017, pp. 3672–3677.
- [8] H. M. La, R. S. Lim, B. B. Basily, N. Gucunski, J. Yi, A. Maher, F. A. Romero, and H. Parvardeh, "Mechatronic systems design for an autonomous robotic system for high-efficiency bridge deck inspection and evaluation," *Mechatronics, IEEE/ASME Transactions on*, vol. 18, no. 6, pp. 1655–1664, Dec 2013.
- [9] H. M. La, N. Gucunski, S.-H. Kee, and L. Nguyen, "Data analysis and visualization for the bridge deck inspection and evaluation robotic system," *Visualization in Engineering*, vol. 3, no. 1, pp. 1–16, 2015.
- [10] H. M. La, N. Gucunski, S. Kee, and L. Nguyen, "Visual and acoustic data analysis for the bridge deck inspection robotic system," in *The 31st International Symposium on Automation and Robotics in Construction and Mining (ISARC)*, July 2014, pp. 50–57.
- [11] H. M. La, N. Gucunski, S.-H. Kee, J. Yi, T. Senlet, and L. Nguyen, "Autonomous robotic system for bridge deck data collection and analysis," in *IEEE Intern. Conf. on Intelligent Robots and Systems (IROS)*, Sept 2014, pp. 1950–1955.
- [12] A. Q. Pham, H. M. La, K. T. La, and M. T. Nguyen, "A magnetic wheeled robot for steel bridge inspection," in *In: Sattler KU, Nguyen D., Vu N., Tien Long B., Puta H. (eds) Advances in Engineering Research and Application. ICERA 2019. Lecture Notes in Networks and Systems, Springer, Cham.*, vol. 104, 2020, pp. 11–17.
- [13] A. Sirken, G. Knizhnik, J. McWilliams, and S. Bergbreiter, "Bridge risk investigation diagnostic grouped exploratory (bridge) bot," in *2017 IEEE/RSJ International Conference on Intelligent Robots and Systems (IROS)*. IEEE, 2017, pp. 6526–6532.
- [14] D. Zhu, J. Guo, C. Cho, Y. Wang, and K. Lee, "Wireless mobile sensor network for the system identification of a space frame bridge," *IEEE/ASME Trans. on Mechatronics*, vol. 17, no. 3, pp. 499–507, June 2012.
- [15] J. Guo, W. Liu, and K.-M. Lee, "Design of flexonic mobile node using 3d compliant beam for smooth manipulation and structural obstacle avoidance," in *2014 IEEE International Conference on Robotics and Automation (ICRA)*. IEEE, 2014, pp. 5127–5132.
- [16] S. Kamdar, "Design and manufacturing of a mecanum wheel for the magnetic climbing robot," *Master Thesis, Embry-Riddle Aeronautical University*, May 2015.
- [17] N. H. Pham and H. M. La, "Design and implementation of an autonomous robot for steel bridge inspection," in *2016 54th Annual Allerton Conference on Communication, Control, and Computing (Allerton)*. IEEE, 2016, pp. 556–562.
- [18] H. M. La, T. H. Dinh, N. H. Pham, Q. P. Ha, and A. Q. Pham, "Automated robotic monitoring and inspection of steel structures and bridges," *Robotica*, vol. 37, no. 5, p. 947–967, 2019.
- [19] A. Q. Pham, C. Motley, S. T. Nguyen, and H. M. La, "A robust and reliable climbing robot for steel structure inspection," in *2022 IEEE/SICE International Symposium on System Integration (SII)*. IEEE, 2022, pp. 336–343.
- [20] C. Motley, S. T. Nguyen, and H. M. La, "Design of a high strength multi-steering climbing robot for steel bridge inspection," in *2022 IEEE/SICE International Symposium on System Integration (SII)*. IEEE, 2022, pp. 323–328.
- [21] W. Shen, J. Gu, and Y. Shen, "Permanent magnetic system design for the wall-climbing robot," in *IEEE International Conference Mechatronics and Automation, 2005*, vol. 4. IEEE, 2005, pp. 2078–2083.
- [22] S. T. Nguyen and H. M. La, "Development of a steel bridge climbing robot," in *2019 IEEE/RSJ International Conference on Intelligent Robots and Systems (IROS)*. IEEE, 2019, pp. 1912–1917.
- [23] G. Lee, G. Wu, J. Kim, and T. Seo, "High-payload climbing and transition by compliant locomotion with magnetic adhesion," *Robotics and Autonomous Systems*, vol. 60, no. 10, pp. 1308 – 1316, 2012.
- [24] T. Seo and M. Sitti, "Tank-like module-based climbing robot using passive compliant joints," *IEEE/ASME Transactions on Mechatronics*, vol. 18, no. 1, pp. 397–408, Feb 2013.
- [25] S. Nguyen and H. La, "A climbing robot for steel bridge inspection," in *Journal of Intelligent & Robotic Systems, Springer Publisher*, vol. 75. IEEE, 2021, p. 102.
- [26] T. Bandyopadhyay, R. Steindl, F. Talbot, N. Kottege, R. Dungavell, B. Wood, J. Barker, K. Hoehn, and A. Elfes, "Magneto: A versatile multi-limbed inspection robot," in *2018 IEEE/RSJ International Conference on Intelligent Robots and Systems (IROS)*. IEEE, 2018, pp. 2253–2260.
- [27] A. Mazumdar and H. H. Asada, "Mag-foot: A steel bridge inspection robot," in *2009 IEEE/RSJ International Conference on Intelligent Robots and Systems*. IEEE, 2009, pp. 1691–1696.
- [28] P. Ward, P. Manamperi, P. R. Brooks, P. Mann, W. Kaluarachchi, L. Matkovic, G. Paul, C. H. Yang, P. Quin, D. Pagano, D. Liu, K. Waldron, and G. Dissanayake, "Climbing robot for steel bridge inspection: Design challenges," in *Austrroads Publications Online, ARRB Group*, 2015.
- [29] S. T. Nguyen, A. Q. Pham, C. Motley, and H. M. La, "A practical climbing robot for steel bridge inspection," in *2020 IEEE International Conference on Robotics and Automation (ICRA)*. IEEE, 2020, pp. 9322–9328.
- [30] H. D. Bui, S. T. Nguyen, U.-H. Billah, C. Le, Tavakkoli, and H. M. La, "Control framework for a hybrid-steel bridge inspection robot," in *2020 IEEE/RSJ International Conference on Intelligent Robots and Systems (IROS)*. IEEE, 2020, pp. 2585–2591.
- [31] A. Q. Pham, A. T. La, E. Chang, and H. M. La, "Flying-climbing mobile robot for steel bridge inspection," in *2021 IEEE International Symposium on Safety, Security, and Rescue Robotics (SSRR)*, 2021, pp. 230–235.
- [32] "Elios2," <https://www.youtube.com/watch?v=hW1Fn32JBIs/>.
- [33] "Case study: Advancing bridge inspections with intel's drone solutions, accessed on February 1, 2021," <https://www.intel.com/content/www/us/en/products/docs/drones/advancing-bridge-inspections-case-study.html>.
- [34] S. T. Nguyen and H. M. La, "Roller chain-like robot for steel bridge inspection," in *the 9th International Conference on Structural Health Monitoring of Intelligent Infrastructure (SHMII-9)*, Aug 2019.
- [35] H. Eto and H. H. Asada, "Development of a wheeled wall-climbing robot with a shape-adaptive magnetic adhesion mechanism," in *2020 IEEE International Conference on Robotics and Automation (ICRA)*. IEEE, 2020, pp. 9329–9335.
- [36] Y. Takada, S. Ito, and N. Imajo, "Development of a bridge inspection robot capable of traveling on splicing parts," *Inventions*, vol. 2, 2017.
- [37] "Bike," <https://inspection-robotics.com/bike/>.
- [38] "Sir," <http://www.sir.ethz.ch/>.
- [39] "Iso3691," <https://www.iso.org/obp/ui/#iso:std:iso:3691:-4:ed-1:v1:en/>.
- [40] "Iec60034," https://global.ihs.com/doc_detail.cfm?document_name=IEC%2060034%2D1.